



HAL
open science

Geophysical investigations at Stromboli volcano, Italy. Implications for ground water flow and paroxysmal activity.

André Revil, Anthony Finizola, Francesco Sortino, Maurizio Ripepe

► **To cite this version:**

André Revil, Anthony Finizola, Francesco Sortino, Maurizio Ripepe. Geophysical investigations at Stromboli volcano, Italy. Implications for ground water flow and paroxysmal activity.. Geophysical Journal International, 2004, 157, pp.426-440. 10.1111/j.1365-246X.2004.02181.x . hal-01452538

HAL Id: hal-01452538

<https://hal.science/hal-01452538>

Submitted on 2 Feb 2017

HAL is a multi-disciplinary open access archive for the deposit and dissemination of scientific research documents, whether they are published or not. The documents may come from teaching and research institutions in France or abroad, or from public or private research centers.

L'archive ouverte pluridisciplinaire **HAL**, est destinée au dépôt et à la diffusion de documents scientifiques de niveau recherche, publiés ou non, émanant des établissements d'enseignement et de recherche français ou étrangers, des laboratoires publics ou privés.

Geophysical investigations at Stromboli volcano, Italy: implications for ground water flow and paroxysmal activity

A. Revil,¹ A. Finizola,^{2,*} F. Sortino³ and M. Ripepe⁴

¹CNRS-CEREGE, Department of Hydrogeophysics and Porous Media, BP-80, F-13545, Aix-en-Provence, Cedex 4, France. E-mail: revil@cerege.fr

²Laboratoire Magmas et Volcans, Université Blaise Pascal, OPGC, CNRS, 5 rue Kessler, 63038 Clermont-Ferrand, France. E-mail: finizola@ov.ingv.it

³Istituto Nazionale di Geofisica e Vulcanologia, Via Ugo La Malfa, 153, 90144 Palermo, Italy. E-mail: sortino@pa.ingv.it

⁴Università di Firenze, Dipartimento di Scienze della Terra, via G. La Pira, 4, I-50121, Firenze, Italy. E-mail: ripepe@ingv.it

SUMMARY

Stromboli volcano (Italy) is characterized by a permanent mild explosive activity disrupted by major and paroxysmal eruptions. These strong eruptions could be triggered by phreato-magmatic processes. With the aim of obtaining a better understanding of ground water flow in the vicinity of the active vents, we carried out a set of geophysical measurements along two profiles crossing the Fossa area (through the Pizzo, the Large and the Small Fossa craters). These measurements include electrical resistivity, induced polarization, self-potential, temperature and CO₂ ground concentration. These methods are used in order to delineate the crater boundaries, which act as preferential fluid flow pathways for the upflow of hydrothermal fluids. The absence of fumarolic activity in the Fossa area and the ground temperature close to 100 °C at a depth of 30 cm indicate that the hydrothermal fluids condense close to the ground surface. Part of this condensed water forms a shallow drainage network (<20 m) in which groundwater flows downslope toward a perched aquifer. The piezometric surface of this aquifer is located ~20 m below the topographic low of the Small Fossa crater and is close (<100 m) to the active vents. Electrical resistivity tomography, temperature and CO₂ measurements show that this shallow aquifer separates the underlying hydrothermal body from the ground surface. Further studies are needed to ascertain the size of this aquifer and to check its possible implications for the major and paroxysmal events observed at the Stromboli volcano.

1 INTRODUCTION

On 2002 December 28–30 important morphological and volcanic activity changes occurred at Stromboli, a volcanic island located in the northern part of the Aeolian arc, in the Tyrrhenian Sea (Fig. 1). (1) Huge sector collapses in the submarine and aerial parts of the edifice were responsible for a small tsunami, which damaged part of the village of Piscità-Scari (Fig. 1). (2) The central and NE craters collapsed. (3) A set of cracks developed through the Fossa area and an effusive activity occurred in the Sciara del Fuoco area on the northwestern flank of the volcano. We report in this paper on a set of new geophysical measurements (including geoelectric studies, temperature and CO₂ measurements) obtained a few months prior to this violent episode. These measurements offer a reference picture from which we can characterize the changes that occurred in the summit part of the volcanic edifice.

Stromboli rises to 924 m above sea level from water depths ranging from 1200 to 2200 m. This volcano is characterized by a persistent rhythmic activity for the last two thousand years. In 2002, this mild explosive activity consisted of violent gas emissions from three active vents and the projection of incandescent scorias and ash over short periods of time (a few seconds) and with a frequency of several events per hour. The explanation of this episodicity has been studied on the basis of a set of laboratory experiments by Jaupart & Vergnolle (1988, 1990), showing the different phases of magma degassing, accumulation of gas in the conduits and finally coalescence of gas bubbles (Ripepe *et al.* 2001). The explosion of these gas bubbles at the top of the magmatic column expels incandescent fragments of lava to distances smaller than ~100 m. In addition to this explosive activity, effusive activity is sometimes observed on the northwestern flanks of the volcano, in the Sciara del Fuoco area. Such activity occurred recently during the last effusive crisis discussed above.

The normal mild explosive activity is sometimes disrupted by major or paroxysmal events (Barberi *et al.* 1993, 2001). During major events (~1–2 events yr⁻¹ over the past century), lava fragments

*Now at: Osservatorio Vesuviano, Sezione INGV-Napoli, Via Diocleziano 328, 80124 Napoli, Italy.

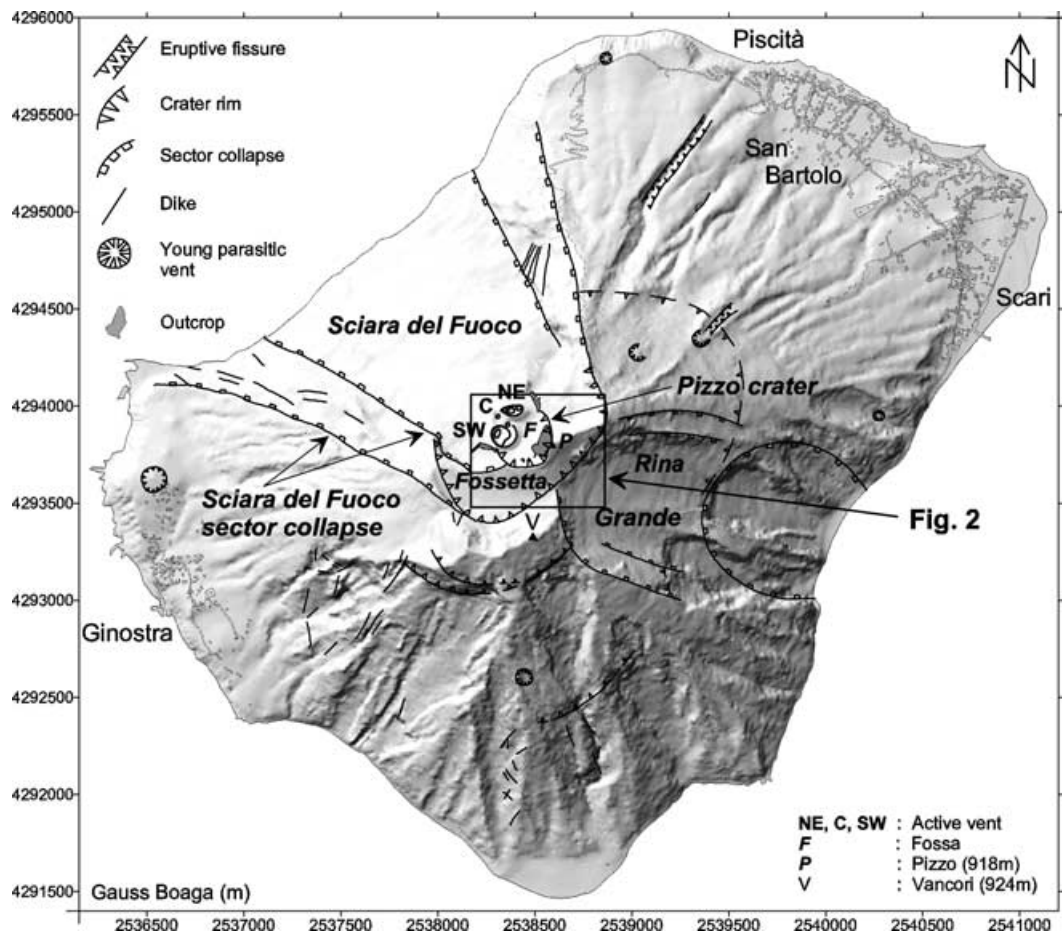


Figure 1. Map of Stromboli island with the location of the studied area.

of metre scale are expelled to several hundreds metres away from the vents (Bertagnini *et al.* 1999). During paroxysmal eruptions, volcanic bombs of several tons are expelled to several kilometres away. 20 major events occurred between 1993 and 2003, the last of which occurred on 2003 April 5. The most important paroxysmal event during the twentieth century occurred on 1930 September 11. During this extremely violent event, volcanic bombs reached a distance of 4 km.

According to Métrich *et al.* (2001), strong explosive events have their origin deep inside the magmatic plumbing system of the volcano. However, Rittmann (1931) observed that the 1930s paroxysm was triggered by two strong phreatic eruptions. It is therefore possible that the origin of the major and paroxysmal eruptions of Stromboli volcano could be associated with phreato-magmatic (shallow or deep) processes as suggested recently by Finizola *et al.* (2003). In this case, these eruptions could be preceded by forced ground water flow and possible electric precursors of electrokinetic origin could be detected (the so-called volcano-electric effect modelled recently by Revil *et al.* 2003). Indeed, the flow of the ground water through a deformable (e.g. brittle thermoporo-elastic) porous body generates remarkable electrical and magnetic field fluctuations, which can be easily detected by a set of sensors (electrodes and magnetometers) located at the ground surface. Such an occurrence of electromagnetic field anomalies at the ground surface of active volcanoes has been very well documented over the last 15 years by volcanologists and geophysicists (e.g. Jackson & Kauahikaua 1987; Aubert & Baubron 1988; Zlotnicki & Le Mouél 1988; Di Maio & Patella 1994; Di Maio *et al.* 1996; Revil *et al.* 2003).

The interpretation of self-potential (SP) signals cannot be used as a stand alone technique. To combine various kinds of geophysical information such as resistivity, self-potential, ground temperature and CO₂ concentration is now a standard technique in geothermal exploration (e.g. Zohdy *et al.* 1973), but is rather new in application to very active volcanoes. In addition, very few geoelectrical investigations have been performed to date at Stromboli volcano, especially in the summit craters (the Pizzo, the Large and the Small Fossa craters, Figs 2 and 3). Ballestracci (1982) was probably the first to carry out a self-potential survey there. He suggested the presence of several hydrothermal convective cells below the Fossa area. Very recently, Finizola *et al.* (2003) mapped self-potential, temperature and CO₂ ground concentration in order to constrain the extent of the hydrothermal system and to understand the pattern of fluid flow in the Fossa area. To complement the work already performed by Finizola *et al.* (2003), we carried out in 2002 May a 2 week campaign of measurements in the Fossa area. These measurements included electrical resistivity, induced polarization, temperature, ground CO₂ concentration and self-potential measurements obtained along two profiles crossing the Large Fossa crater. In the following we will use the terminology and nomenclature defined by Finizola *et al.* (2003).

The purpose of the present study is to infer two types of information from this new data set. The former is structural information related to discontinuities such as crater boundaries and volcanic deposits. The other concerns the determination of the pattern of ground water flow inside and in the vicinity of the Large Fossa crater, especially the detection of possible perched aquifers in the vicinity of the

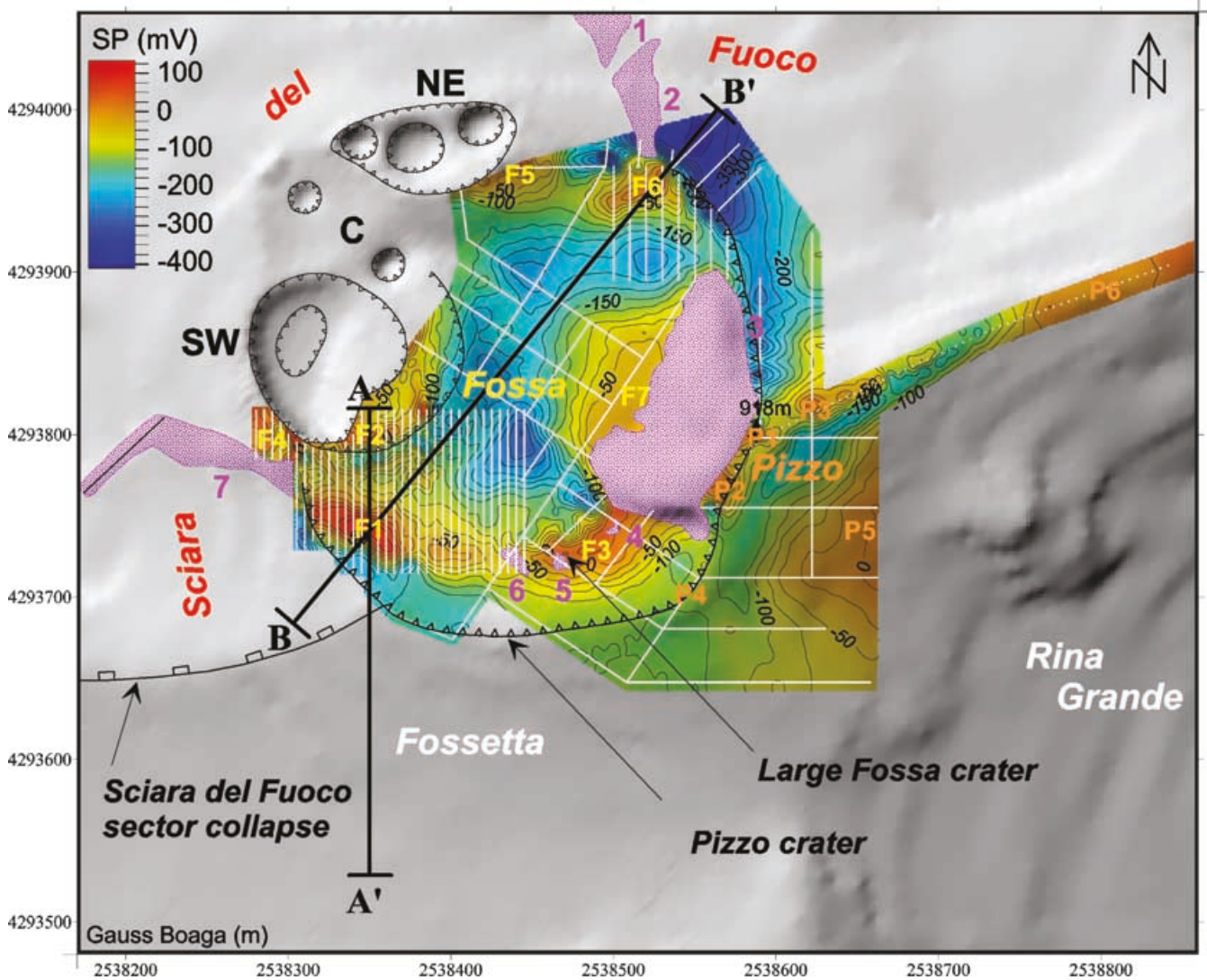


Figure 2. Map of the Fossa area with the high-resolution self-potential survey made by Finizola *et al.* (2003) and the location of the two profiles investigated in the present study. SW (southwest), C (central) and NE (northeast) stand for the three active vents located into the Fossa area before the eruption of 2002 December.

active vents. Indeed, the presence of such aquifers could occasionally be responsible of the major and paroxysmal eruptions observed at Stromboli through phreato-magmatic interactions.

2 DATA ACQUISITION

Direct current electrical resistivity measurements (Wenner- α) were obtained along the two straight profiles shown in Figs 2 and 3 using a set of 64 brass electrodes to reduce polarization effects. The spacing between the electrodes in the field was 5 m along the ground surface. The first electrical resistivity profile AA' (315 m long) stretched from the north to the south. The second profile BB' stretched from the southwest to the northeast (Fig. 2). Profile BB' was 430 m long along the curvilinear coordinate and required a roll-over of the electrodes.

Electrical resistivity tomographies (ERTs) were obtained using RES2DINV, the software by Loke & Barker (1996), which uses a finite-element grid for the forward analysis. Topography was included in the inversion. The results are shown in Figs 4 and 5. Note

that in this preliminary study only 2-D resistivity profiles could be carried out owing to the time and danger of staying too long inside the Fossa area. Accounting for the complex geometry of the Fossa craters and hydrothermal body, it is absolutely clear that only 3-D tomographies could help to distinguish the complex structural heterogeneities present inside the Fossa area. However, we show below that 2-D-ERT already indicate a great number of details compatible with the other data obtained at the ground surface (e.g. the self-potential, temperature and CO₂), especially in terms of the hydrothermal fluid flow pattern.

Temperature measurements were obtained using thermal probes placed at a constant depth of 30 cm with a spacing equal to 2.5 m along profiles AA' and 5 m along profile BB'. The method is fully described by Finizola *et al.* (2003) and is summarized here. At each measurement station, a hole was set up with a steel rod. Then, a temperature probe encapsulated in a graduated wood stick was pushed in the hole at 30 cm. The ground was compacted around the wooden stick. Readings were taken with a digital thermometer to the nearest 0.1 °C. Thermal equilibrium was achieved in less than ~20 min after the installation of the thermal probes. Fig. 6 shows that the

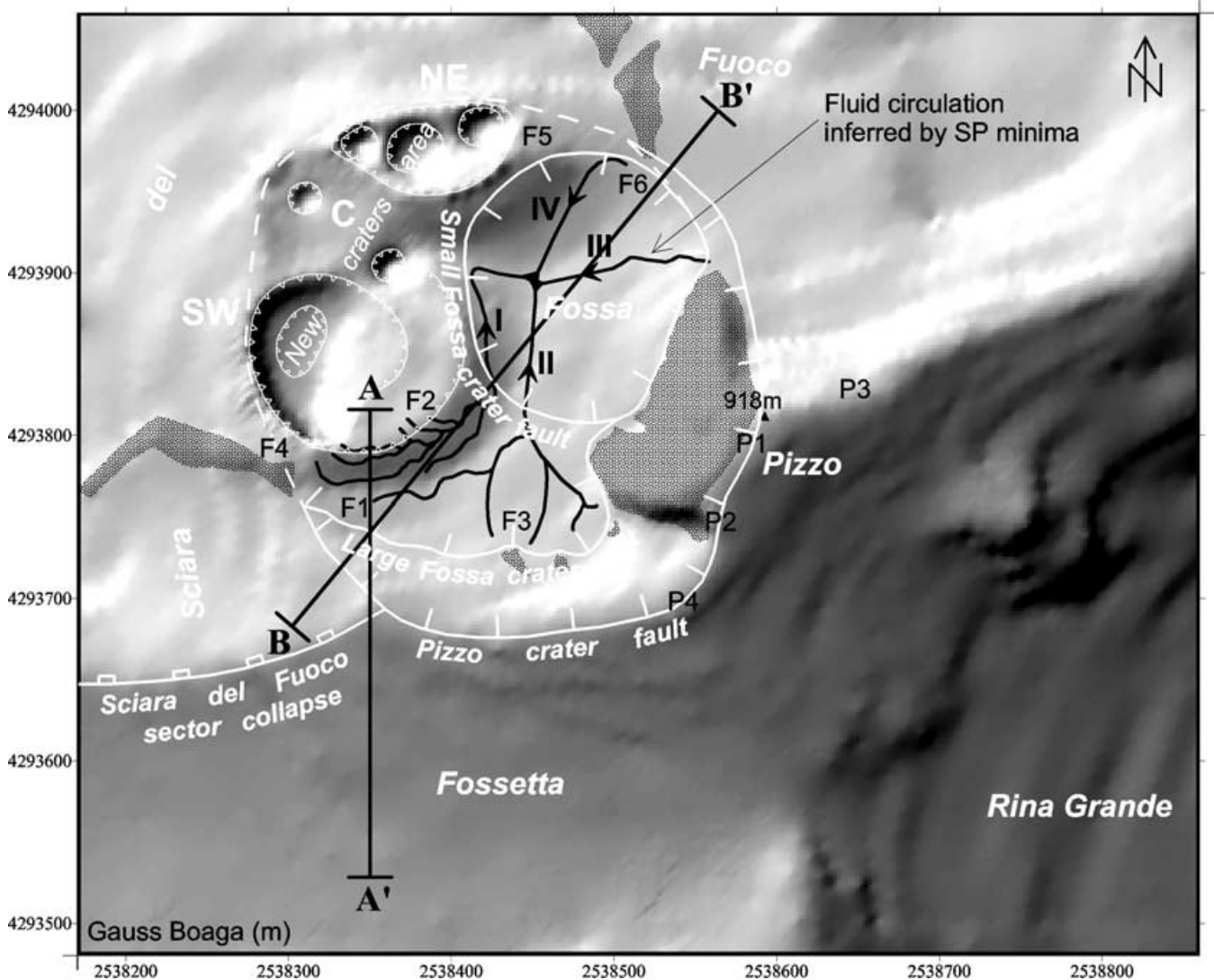


Figure 3. Structural limits of the Fossa area. F1–F6 and P1–P4 correspond to the position of the thermal anomalies determined by Finizola *et al.* (2003) in the Fossa (F) and the Pizzo (P) areas, respectively. The lines correspond to the drainage network of shallow ground water circulation below the Fossa inferred by SP minima. This drainage network originates in thermal anomalies where hydrothermal steam condenses just below the ground surface. The network of channels converges toward the topographic low of the Fossa, inside the rims of the Small Fossa Crater, to supply a perched aquifer.

diurnal temperature variation at 30 cm depth was $\sim 1^\circ\text{C}$, which is considered to be a rough estimate of the uncertainty associated with these temperature measurements.

Self-potential measurements were spaced each metre along profile AA' and each 2.5 m along profile BB'. We used a pair of non-polarizable Cu/CuSO₄ electrodes. The difference of electrical potential between the reference electrode (arbitrarily placed at the beginning of the profile) and the moving electrode was measured with a high impedance voltmeter (the impedance of the ground was, in most cases, $< 200\text{ k}\Omega$, much below the internal impedance of the voltmeter $\sim 100\text{ M}\Omega$). At each station, a small hole ($\sim 10\text{ cm}$ deep) was dug to improve the electrical contact between the electrode and the ground. No water was added to the ground because the electrical contact between the electrodes and the ground was found to be excellent for all the stations due to the good level of moisture. A possible source of errors is considered to be related to the drift at the electrodes with time due to chemical reactions between the electrodes and the surrounding material. We checked that the drift between the two electrodes put face-to-face was smaller than

2 mV at the end of each profile (the duration of acquisition of the self-potential data was roughly 1 h for each profile).

3 SOURCES OF SP AND CO₂ ANOMALIES

Two main sources of electrical current can generate low-frequency or quasi-static electrical potential signals in a volcanic system. They are: (1) the electrokinetic (or hydroelectric) coupling associated with ground water flow and (2) the thermoelectric effect associated with chemical potential gradients of the ions contained in the pore water in the presence of a temperature gradient. However, despite the fact that self-potential and temperature signals are closely related, as shown below, the intensity of the thermoelectric effect is extremely small in porous materials (less than a few tenths of $\text{mV } ^\circ\text{C}^{-1}$). Therefore, the thermoelectrical coupling can be ruled out as the source of this correlation. To avoid misconceptions concerning the nature of the source, we term 'thermoelectrokinetic effects'

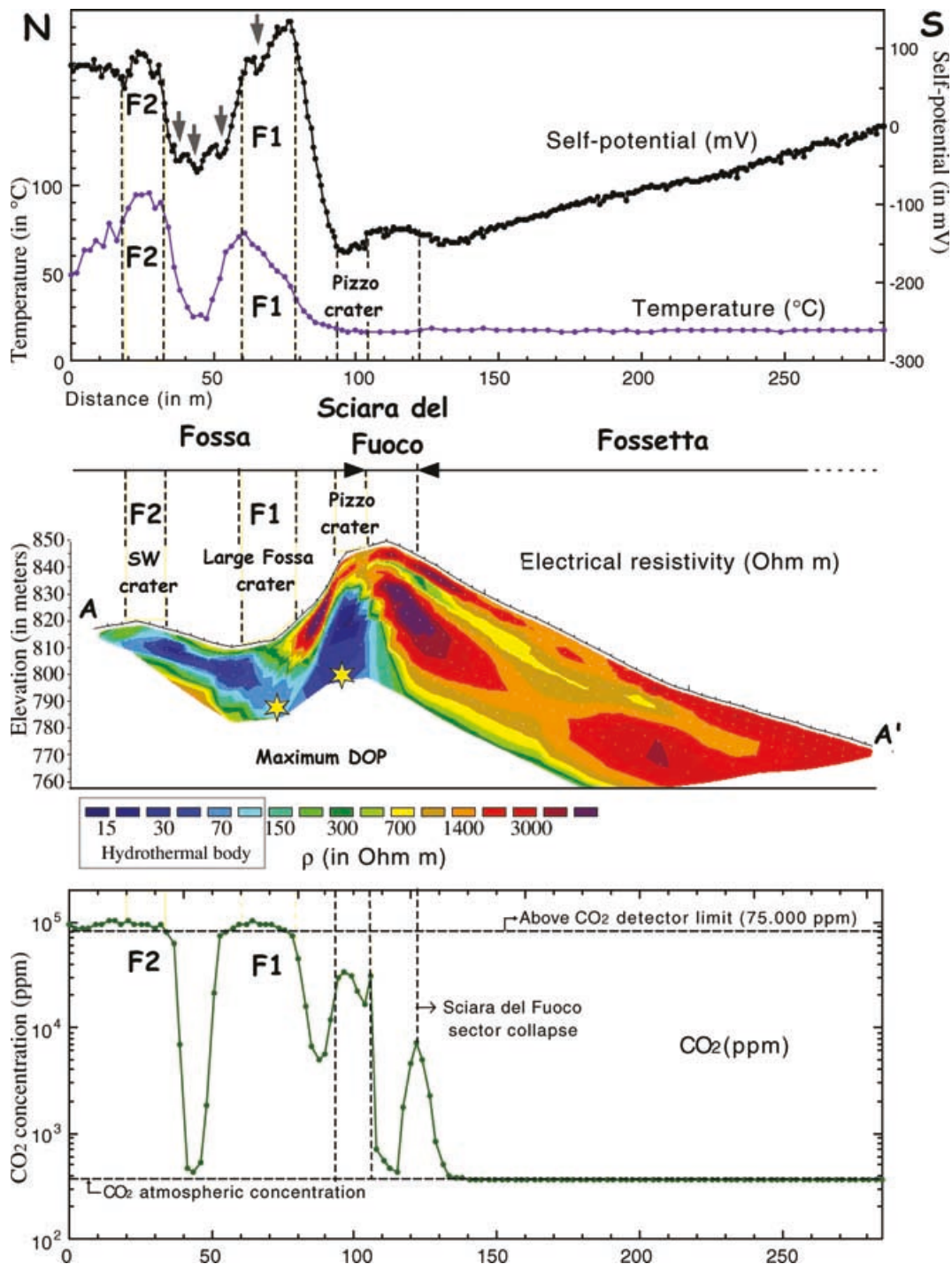


Figure 4. Temperature, self-potential, electrical resistivity and CO₂ ground concentration along the AA' profile. Note the correlation between these parameters indicating the presence of a shallow hydrothermal system characterized by a high electrical conductivity in the ground (the stars indicate the maxima of the SP-dipole occurrence probability, DOP, see Fig. 11).

the self-potential signals associated with the upflow of hydrothermal fluids. The various electrokinetic sources responsible for the occurrence and pattern of the observed self-potential signals are discussed further in Section 4.3. Note that the correlation between the self-potential signals and temperature measurements was not an artefact of the measurements because: (1) the self-potential data were obtained at the ground surface where no fumarolic activity was observed (so the electrode quality was not altered by active chem-

istry); (2) temperature measurements were made at a depth of 30 cm, the temperature being roughly constant at the ground surface; (3) the quality of the scanning electrode was checked after the completion of each profile to test that no drift had occurred between the two electrodes during the acquisition of the measurements.

We also observed small variations of the self-potential signals with time (Fig. 7). However, the amplitude of this variation was much smaller than the spatial amplitude of the self-potential signals

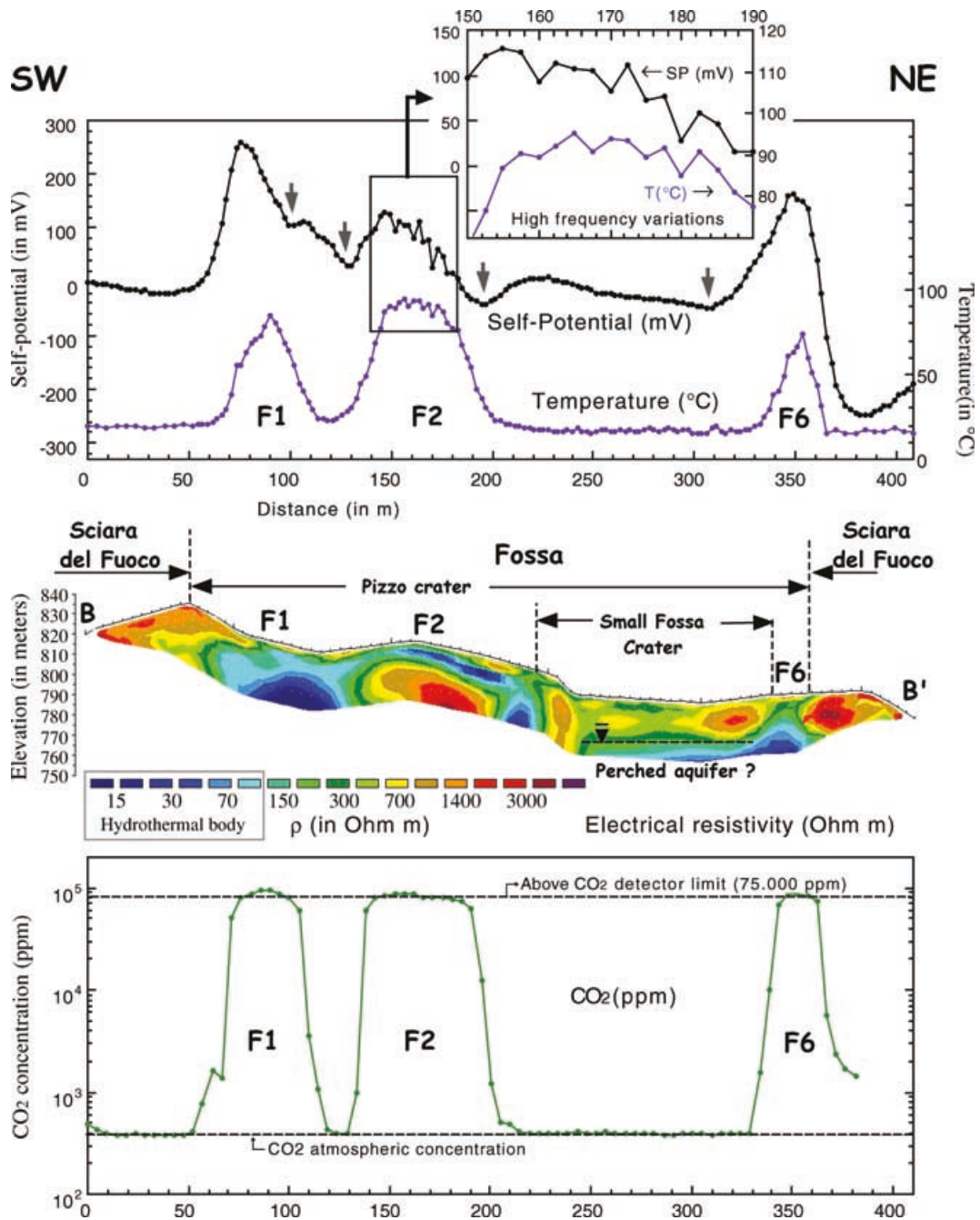


Figure 5. Temperature, self-potential, electrical resistivity and CO₂ ground concentration along the BB' profile. The CO₂ anomaly associated with temperature and self-potential anomalies is correlated with the presence of a conductive body contouring a resistive body. This conductive body corresponds to the pathways for the hydrothermal fluids.

reported in Figs 2, 4 and 5. The origin of these self-potential variations with time could be explained by either variation in capillary flow in the non-saturated zone (e.g. Perrier & Morat 2000) or atmospheric electrical variations (in particular the 'normal' electrical field and the 'induced' telluric field, e.g. Trique *et al.* 2002). The magnitude of these effects is in the range 10–100 $\mu\text{V m}^{-1}$ for the diurnal variation on solar quiet days and can be of the order of several hundred $\mu\text{V m}^{-1}$ during magnetic storms (Ole Hanekop, Pers. comm., 2002). So a dipole of 200 m can record some diurnal variations between 2 and 20 mV, which is the order of magnitude of the time variation recorded here (~ 10 mV). The influence of these di-

urnal variations on a self-potential monitoring network is discussed later in Section 4.2.

The CO₂ measurements (Figs 4 and 5) were obtained at the end of 2002 October. They measured in the field with a spacing of 2.5 and 5 m along profiles AA' and BB', respectively. Gas was pumped through a tube (2 mm in diameter) made of copper, which was inserted into the ground at a depth of 0.5 m. The CO₂ concentrations were obtained as a difference of potential after calibration of the infrared photoelectric cell (uncertainty <5 per cent). Values >75 000 ppm were discarded because they reach the saturation of the calibration curve. Carbon dioxide anomalies (i.e. carbon dioxide

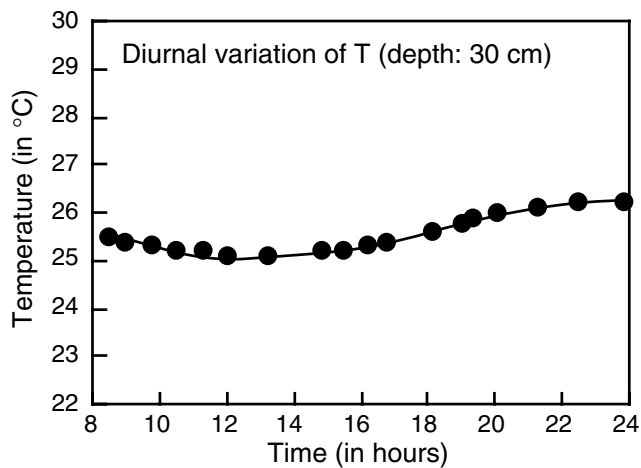


Figure 6. Diurnal variation of the temperature at 30 cm depth in the ground (the starting time is 8:00 AM, GPS time, 2002 August).

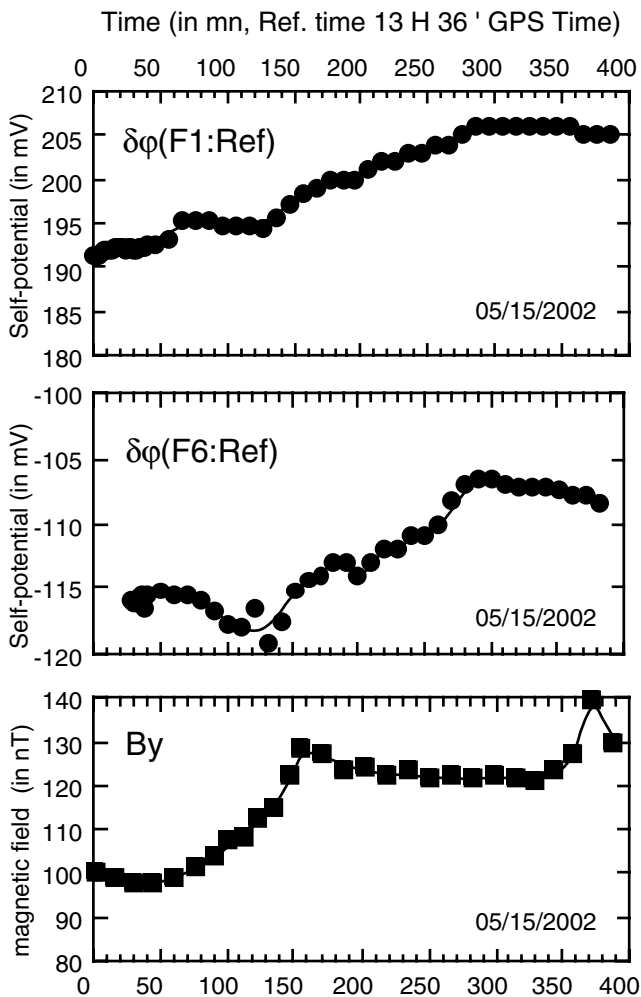


Figure 7. Self-potential variations at thermal anomalies F1 and F6 recorded over several hours. The reference electrode is taken in the Fossetta (the dipole F1-Ref is approximately south–north, length ~200 m). Magnetic data from www.intermagnet.org measured at the Aquila magnetic observatory. The B_y -component (east–west) is related to the x -component of the induced electric field.

levels recorded above the atmospheric concentration, ~330 ppm) find their origin in the high CO_2 concentration rate associated with the degassing of magma inside the volcanic system. The gas is then conveyed up with the upflow of hydrothermal fluids providing information concerning the plumbing system of the hydrothermal body. CO_2 is very sensitive measurement to delineate crater boundaries, which act as preferential fluid flow pathways for the hydrothermal fluids.

4 STRUCTURAL AND HYDROGEOLOGICAL SETTINGS

4.1 Structural background of the Fossa area

The Fossa is surrounded by a continuous topographic rim called the Pizzo crater, which displays a circular shape of ~350 m in diameter and is delimited toward the east, south and northwest by the Pizzo, the Fossetta and the Sciara del Fuoco areas, respectively (Figs 1 and 2). The rim between the Fossetta and the Sciara del Fuoco area corresponds to the limit of the Sciara del Fuoco sector collapse (Figs 1 and 2). Inside the Pizzo crater, two other crater rims have been identified by Finizola *et al.* (2003). There are: (1) the Large Fossa crater, 280 m in diameter, bordered by a sharp positive self-potential anomaly (Fig. 4) and (2) the Small Fossa crater located inside the Large Fossa crater (Fig. 4). The latter is 150 m wide and is centred just around the topographic low of the Fossa. It is characterized by low temperature values and no anomalous ground CO_2 concentration. This implies that the Small Fossa crater is sealed from the underlying hydrothermal system by an impermeable layer, which impedes the upflow of hot hydrothermal fluids and CO_2 . Part of the rims of the Large Fossa and Small Fossa craters represent preferential pathways for the upward outflow of hydrothermal fluids. This explains why they are outlined by both temperature, CO_2 and self-potential anomalies. These preferential fluid flow pathways are probably associated with a network of open cracks and fractures located along the lithological discontinuities of crater boundaries.

4.2 Interpretation of electrical resistivity

Two main types of rocks are present at the ground surface in the Fossa area. They are tephra (strombolian scoriae) and pyroclastites outcrops (see 3–6 in Fig. 2). The electrical resistivity depends on a number of parameters, which makes, in principle, its interpretation in terms of lithology rather difficult. These parameters include the water content, the ionic charge of the pore water, the presence of alteration products (such as clay minerals and zeolites) and the temperature. It follows, in principle, that there is no direct relationship between lithology and electrical resistivity. Nevertheless, changes in lithology, especially in rock permeability drastically modify the related phenomena such as: (1) the water content, (2) the water–rock interactions and the rock alteration, and (3) the thermal convection processes and temperature, and then, consequently lithology influences electrical resistivity.

Low electrical resistivity observed in the resistivity cross-sections ($<200 \Omega \text{ m}$) coincides with temperature, self-potential and CO_2 anomalies observed at the ground surface (Figs 4 and 5). So these low electrical resistivity values can be associated with permeable zones where uprising hot fluids escape preferentially. For example, thermal anomalies F1 and F2 have their low-resistivity counterparts in both profiles AA' and BB'. Temperature influences strongly the electrical resistivity of rocks (e.g. Llera *et al.* 1990) and, as a result,

large resistivity contrasts (\sim one order of magnitude) exist between a hydrothermal reservoir characterized by low electrical resistivity and the surrounding formations. However, this cannot by itself explain the very large contrasts of electrical resistivity shown in profiles AA' and BB' with electrical resistivity of the hydrothermal body $\sim 10\text{--}50 \Omega \text{ m}$ while the electrical resistivity of the surrounding body is usually $> 1000 \Omega \text{ m}$. The high salinity of the hydrothermal brines, the presence of cracks and/or the high porosity of the permeable rock probably play additional roles.

Along profile AA', two sharp resistivity changes correspond to the Pizzo and Large Fossa crater boundaries (Fig. 4). This pattern displays the stratigraphic succession and the chronology of the apparition of the Pizzo and Large Fossa craters very well. Along profile BB', two sharp resistivity contrasts are located at both ends of the profile. They correspond in both cases to the topographic highs separating the Fossa and the Sciarra del Fuoco areas (Figs 1 and 2). They represent the boundaries of the Pizzo crater. The three thermal anomalies F1, F2 and F6 recorded at the ground surface, also have their shallow conductive counterparts. Between anomalies F1 and F2, we observe a horizontal conductive body located at a depth of $\sim 5\text{--}10 \text{ m}$. This conductive body corresponds to the shallow water drainage identified by the SP minima in the self-potential map (Fig. 2). Between anomalies F2 and F6, we interpret the horizontal conductive body located at $\sim 30 \text{ m}$ below the ground surface as a perched aquifer. Indeed, this structure is located in the area of convergence of the drainage network channelling water inside the Small Fossa crater (Fig. 3). The electrical resistivity of this aquifer is $\sim 50 \pm 20 \Omega \text{ m}$. In the laboratory, we have measured a pore water conductivity of $\sigma_f = 0.1 \text{ S m}^{-1}$ when distilled water is mixed and equilibrated with volcanic ashes (see Section 4.4). Archie's law with an average porosity ϕ of 0.50 (50 per cent) yields a rock resistivity $\rho = 1/(\phi^2 \sigma_f) = 50 \Omega \text{ m}$ in agreement with the field value. The presence of this perched aquifer will require confirmation from deeper ERTs with a larger spacing between the electrodes.

4.3 The origin of self-potential signals

Finizola *et al.* (2002, 2003) obtained a self-potential map at the scale of the whole Stromboli island and a high-resolution self-potential map at the scale of the Fossa area (shown in Fig. 2). The new self-potential profiles obtained in 2002 May along profiles AA' and BB' are shown in Figs 4 and 5. A close inspection between both two data sets indicates that the main self-potential anomalies were stable over several years before the event of 2002 December.

The self-potential data appear as the superposition of signals of different spatial wavelengths. We observe large positive self-potential anomalies extending over tens of metres. These anomalies are correlated with temperature and ground CO_2 anomalies. They correspond to electrokinetic signals associated with the upflow of hydrothermal fluids. These positive self-potential anomalies correspond to the 'thermo-electrokinetic effect' discussed above (Section 3). Smaller wavelengths ($\sim 5\text{--}10 \text{ m}$) correspond to drainage structure channelling ground water downslope toward the perched aquifer located just below the topographic low of the Fossa (Figs 3 and 5). In addition, there are some areas with a high frequency of spikes in the self-potential signals ($\sim 1 \text{ m}$). These signals are well correlated with high-frequency spatial variations in the temperature (Fig. 5 and Finizola *et al.* 2003). We do not understand the origin of these spikes at present.

To understand the origin, polarity and magnitude of the different signals, it is useful to first discuss the various electrokinetic

contributions playing a role in these signals. The Darcy (filtration) velocity \mathbf{u} (in m s^{-1}) is defined as the volume of water flowing per unit surface area and unit time through a permeable rock. The current density \mathbf{j} (in A m^{-2}) represents the amount of charge passing per unit surface area and unit time through a section of the rock. The Darcy velocity and the electrical current density actually form two coupled equations in porous materials. The physics of this coupling has been discussed in many papers, e.g. Bernabé (1998) and Yoshida (2001) for different and complementary aspects of the problem.

If no external electrical field is applied, the hydraulic and electrical fluxes can be partially decoupled, i.e. in most cases the influence of the electrical field upon the Darcy velocity (electro-osmosis) can be safely neglected. The electrical current density \mathbf{j} is given by the sum of Ohm's law (conductive term) plus a convective source current density (e.g. Bernabé 1998; Trique *et al.* 1999; Revil 2002b; Trique *et al.* 2002):

$$\mathbf{j} = \sigma \mathbf{E} - L(\nabla_p - \rho_f \mathbf{g}) = \sigma \mathbf{E} + \mathbf{j}_s, \quad (1)$$

where $\mathbf{E} = -\nabla\varphi$ is the electrical field (φ is the electrical potential), σ is the electrical conductivity of the porous rock (and not the conductivity of the interstitial water), L is an electrokinetic coupling term (in $\text{m}^2 \text{ V}^{-1} \text{ s}^{-1}$), p is the pore fluid pressure, ρ_f is the mass density of the pore water and \mathbf{g} is the acceleration due to gravity. In eq. (1), \mathbf{j}_s (in A m^{-2}) represents the source current density (streaming current). Using Darcy's law $\mathbf{u} = -(k/\eta_f)(\nabla_p - \rho_f \mathbf{g})$, the source current density \mathbf{j}_s is proportional to the filtration velocity:

$$\mathbf{j}_s = \frac{L\eta_f}{k} \mathbf{u}. \quad (2)$$

In hydrothermal systems, two types of flow dominate. The first is related to piezometric head gradients in confined or unconfined aquifers (hydrostatic contribution). The other contribution is related to the sum of convective effects (associated with temperature gradient and concomitant fluid density variations) and forced flow (associated with fluid pressure in excess of hydrostatic). It follows that the Darcy velocity can be split into two contributions, $\mathbf{u} = \mathbf{u}_0 + \mathbf{u}_1$, where \mathbf{u}_0 represents the contribution associated with piezometric head variation (hydrostatic contribution) and \mathbf{u}_1 is related to excess fluid pressure above hydrostatic (forced flow) plus convective effects. In the present situation, \mathbf{u}_0 corresponds to downslope flow of the condensed steam, whereas \mathbf{u}_1 corresponds to the upflow of hydrothermal fluids. So, according to eq. (2), the electrical current source density can also be split into two terms $\mathbf{j}_s = \mathbf{j}_0 + \mathbf{j}_1$, where \mathbf{j}_0 and \mathbf{j}_1 represent the two contributions associated with \mathbf{u}_0 and \mathbf{u}_1 , respectively. The contribution \mathbf{j}_1 corresponds to the thermo-electrokinetic effect discussed above in Section 3. In both cases, the electrokinetic effect represents a dipolar separation of charge at the local scale and a volume distribution of the source current in a source volume Ω .

For an unconfined aquifer, the electrical potential distribution associated with the contribution \mathbf{j}_0 can be represented as a double layer distribution of charge lying on the piezometric surface (Fournier 1989; Revil *et al.* 2003a). This double layer is simply related to a volume density of dipoles resulting from ground water flow associated with piezometric head variations. The second distribution represents a volume distribution of dipoles used to model the positive self-potential anomalies associated with the upward migration of hot vapour/water through the hydrothermal system. Poldini (1938) showed that the upward flow of water confined within a porous column produces a positive self-potential signal at the top surface of the column with respect to an arbitrary distant reference at the ground surface.

In the quasi-static limit of the Maxwell equations, it follows that the total contribution to the electrical potential at the observation point P is the sum of all the contributions contained in the half-conducting space below the ground surface. This yields:

$$\begin{aligned} \varphi(P) = & \frac{C'}{2\pi} \int_{\partial\Omega} (h - h_0) \left(\frac{\mathbf{r} \cdot \mathbf{n}}{r^3} \right) dS \\ & + \frac{1}{2\pi} \int_{\Omega} \frac{\rho \nabla \cdot \mathbf{j}_1}{r} dV + \frac{1}{2\pi} \int_{\Omega} \frac{\mathbf{E} \cdot \nabla \rho}{r \rho} dV, \end{aligned} \quad (3)$$

where \mathbf{n} is the outward normal to the water table, dS is a surface element of the water table, h is the piezometric head at the source point M , h_0 is the piezometric head from a reference level (datum) where the reference is taken for the electrical potential, ρ is the electrical resistivity, C' represents an electrokinetic coupling coefficient described below, and $\mathbf{r} \equiv MP$ represents the distance between the source point M and the observation point P . In eq. (3), the first term corresponds to the contribution associated with fluid flow below the water table and controlled by piezometric head variations. The second term corresponds to fluid flow associated with excess fluid pressures above hydrostatic levels plus convective effects. The third component is due to the influence of the electrical resistivity distribution upon the equipotentials surfaces. This term is called the 'secondary' source term where the two other sources are 'primary' source terms.

The electrokinetic coupling coefficients C and C' arising in the electrokinetic coupling problem are defined by

$$C \equiv \left(\frac{\partial \varphi}{\partial p} \right)_{j=0} = -L/\sigma, \quad (4)$$

$$C' \equiv \left(\frac{\partial \varphi}{\partial h} \right)_{j=0} = \rho_f g C. \quad (5)$$

The coefficient C represents the classical streaming potential coupling coefficient measured in the laboratory (e.g. Revil 2002b) and C' represents the sensitivity coefficient of the electrical potential with the piezometric head. Laboratory experiments have been performed to determine the order of magnitude of the streaming potential coupling coefficient C for samples taken from the Fossa area. The samples are saturated with NaCl electrolyte at different ionic strengths. The results are shown in Fig. 8. The results indicate that the coupling coefficient depends strongly on the electrical conductivity of the pore water saturating its connected porosity as expected from the theory. It varies typically between -5 to -5000 mV MPa $^{-1}$ depending on the salinity of the pore water.

Jouniaux *et al.* (2000) showed that the water conductivity in equilibrium with volcanic rock samples from Mount Pelée is in the range 0.2–2 mS m $^{-1}$, depending on the mineralogical composition of the sample. We placed demineralized pore water in contact with volcanic ashes collected in the Fossa area. The electrical conductivity was monitored over several days indicating that it reached equilibrium in less than 2 d. We obtained a water conductivity value in equilibrium with the volcanic ash of 0.1 S m $^{-1}$, which is much higher than that obtained by Jouniaux *et al.* (2000). This pore water conductivity was then used to determine the electrokinetic coupling coefficient from the trend shown in Fig. 8. This yields $C' \approx -0.35$ mV m $^{-1}$ (~ -35 mV MPa $^{-1}$) for water saturated conditions. This value is within the range of values determined by Jouniaux *et al.* (2000) for the Mount Pelée volcano (-25 to -410 mV MPa $^{-1}$) accounting for the conductivity of the pore water at this volcano. Note that the pH at equilibrium with the volcanic ashes from the Fossa area and with the atmosphere is 6.5 ± 0.3 (Fig. 8), which is very close to the value reported by Jouniaux *et al.* (2000) for the Mount

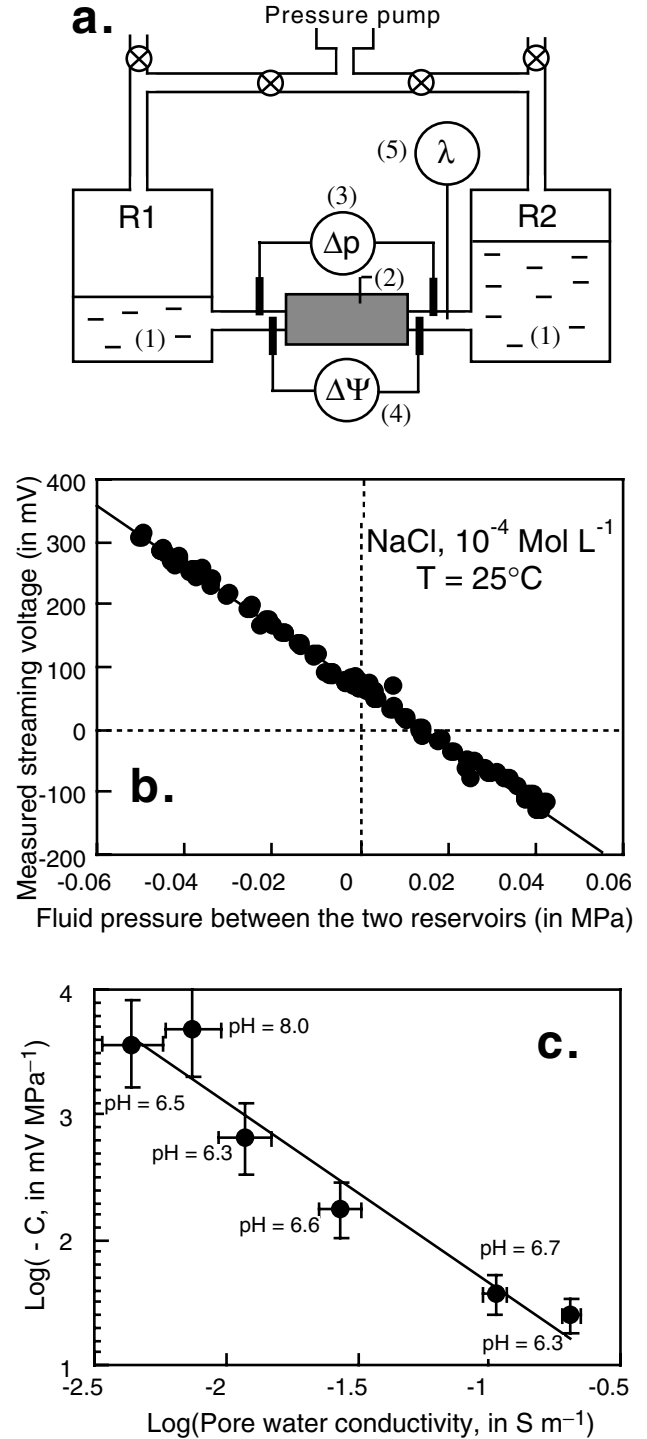


Figure 8. Laboratory measurements of the electrokinetic coupling coefficient. (a) Sketch of the experimental setup (ZetaCadTM). (1) Pore fluid reservoirs R1 and R2; (2) sample tube; (3) pressure sensors, (4) voltage electrodes connected to an impedance meter; and (5) measurements of the electrical conductivity of the electrolyte. The pressure level in the reservoirs is controlled by adjusting the pressure with nitrogen gas. (b) Laboratory measurement of the electrokinetic coupling coefficient. (c) Streaming potential coupling coefficient versus pore water electrical conductivity. The pH values given on the graph represent the pH of the solution in equilibrium with the scoria and measured at the end of the electrokinetic measurements. The relationship between the coupling coefficient and the electrical conductivity of the ground water is $\log_{10}(-C) = 0.23 - 1.44 \log_{10} \sigma_f$, where C is expressed in mV MPa $^{-1}$.

Pelé volcano (pH of 6.4). For unsaturated conditions, the magnitude of the streaming potential coupling coefficient is expected to be higher. Taking $C' = -100 \text{ mV MPa}^{-1}$ and an overpressure source of 2 MPa at 200 m depth (the estimated depth of the heat source reservoir) yields an anomaly of 200 mV, a magnitude similar to that measured in the Fossa area (Figs 4 and 5).

In a very recent paper, Lewicki *et al.* (2003) found a good correspondence between the self-potential, CO_2 and temperature anomalies on the Masaya volcano (Nicaragua). They proposed that this correlation could be primarily attributed to the rapid fluid disruption (RFD) process tentatively described by Johnston *et al.* (2001). However, it should be stressed that the paper by Johnston *et al.* (2001) does not allow one to distinguish between competing effects (Revil 2002a). In addition, the data obtained by Johnston *et al.* (2001) could represent just an artefact due to the fact that the self-potential is measured between two electrodes at two different temperatures and the authors did not performed blank tests and temperature corrections on their data. The data Lewicki *et al.* (2003) can be explained in terms of an electrokinetic mechanism should have created a polarized path along their fault system with a typical self-potential distribution at the ground surface. We could question why the electrokinetic effect should have created such a polarization path and not the RFD mechanism. Eq. (A14) shows that the electrokinetic effect can explain the self-potentials obtained by Lewicki *et al.* (2003) both in terms of strength and distribution without invoking any RFD mechanisms.

We now return to the interpretation of the self-potential signals in the Fossa area. The small minima reported for example in Figs 4 and 5 (see the arrows along the self-potential profiles) are related to the downflow of the ground water. Indeed, the drainage network characterized by a higher hydraulic transmissivity has a typical signature of negative self-potential anomalies along sections perpendicular to the axis of preferential fluid flow (Fig. 9). The distribution of these minima can be interconnected to draw a map of ground water flow in the Fossa crater (Fig. 2) as done by Finizola *et al.* (2003) according to the empirical method developed by Maurice Aubert and co-workers (Aubert *et al.* 1993; Aubert & Atangana 1996; Boubekraoui *et al.* 1998; Aubert & Dupuy 2000). This map shows that the drainage network takes its roots in areas of thermal anomalies (these anomalies are designed by F1, F2, F3 and F6) as shown in Fig. 2. Water condenses from steam just below

the ground surface (there is no fumarolic activity observed in the Fossa area). Then ground water migrates at very shallow depths (<10 m according to the width of these self-potential signals). It is remarkable to observe that the drainage channels converge toward the topographic low of the Small Fossa crater. This indicates that water accumulates potentially in a perched aquifer corresponding to the conductive body shown in Fig. 5 inside the Small Fossa crater. However, additional geophysical investigations are required to confirm this point of view, in particular, deeper 3-D electrical resistivity tomographies.

4.4 Tomography of self-potential

The large self-potential positive anomalies observed over the thermal zones arise from the electrokinetic effect associated with the upward-moving waters resulting from convective or forced flow in the hydrothermal systems. A similar pattern is discussed by Zohdy *et al.* (1973) at the Mud Volcano area in Yellowstone National Park (USA) above a vapour-dominated geothermal system and by Poldini (1938), who used laboratory experiments.

A dipolar tomography algorithm is discussed in the Appendix where the electrical potential measured at the ground surface is analysed to recover the dipolar occurrence probability (in the terminology of Patella 1997) of the source location of the dipole responsible for this anomaly (Fig. 10). We apply this method to the self-potential profile AA' in order to look for the source depth of the self-potential anomaly recorded at the ground surface (Fig. 11). The source is located at a depth of ~ 40 m below the ground surface in one of the low-resistivity zones shown in Fig. 4. However, we have to be very prudent concerning the interpretation of such an algorithm. Indeed, the self-potential signal associated with steady-state ground water flow in a confined aquifer (such as the present hydrothermal body) cannot generate self-potential at the ground surface except at the outflow (or inflow) areas (see the Appendix). Therefore, at least, self-potential mapping demonstrates the areas of outflow of the hydrothermal system very clearly. At best, the source location of the heat source can be obtained through the tomographic algorithm described in the Appendix, but further studies need to be carried out in the laboratory (e.g. through sand-box experiments) to check the reliability of this approach.

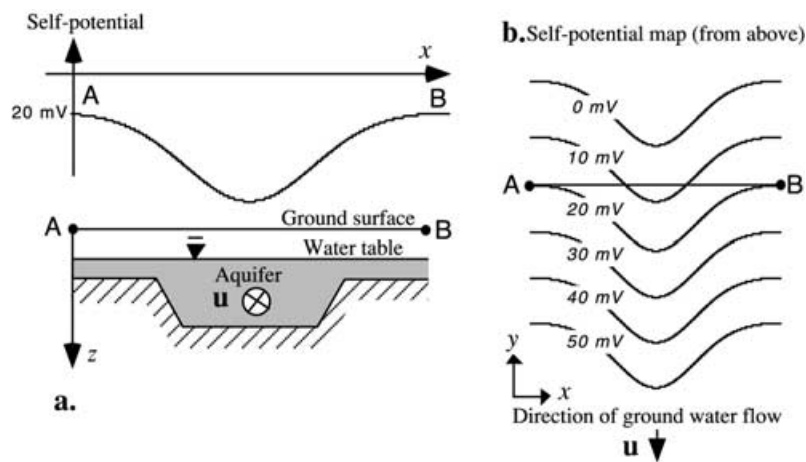


Figure 9. A drainage channel characterized by a high hydraulic transmissivity in an unconfined aquifer produces a negative self-potential anomaly along an axis perpendicular to the ground water flow (\mathbf{u} is the Darcy velocity). (a) Vertical sketch of the drainage channel. (b) Self-potential map observed at the ground surface (note that the electrokinetic coupling produces an electrical field in the direction of the ground water flow).

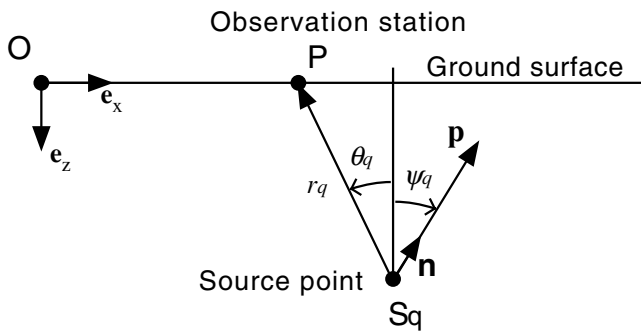


Figure 10. We note \mathbf{p} the dipolar moment of the source point S_q and P an observation station located at the ground surface. For electrokinetic sources, the dipolar moment is in the direction of ground water flow, which depends in turn on the pore fluid pressure gradient.

4.5 Temperature and CO₂ patterns

The temperature profiles shown in Figs 4 and 5 indicate huge geothermal gradients in the first decimetres below the ground surface (the temperature drops from 25 to 90 °C over a depth interval of 30 cm). The distribution of the temperature T in the porous medium obeys the energy conservation law combined with a constitutive flux equation including both conductive and convective terms. There is also a direct correlation observed between the flux of CO₂ (and CO₂ ground concentrations above the atmosphere concentration) and the heat flux. This is due to the fact that CO₂ is primarily conveyed by forced ground water flow associated with the upsurge of

hydrothermal fluids at the rims of the craters plus diffusion under concentration gradients. Therefore, the concentration of CO₂ obeys laws similar to those given for the temperature.

The fact that the convective transport represents the dominant transfer mechanism for electrical current (electrokinetic source), heat flow and CO₂ explains the similarities between these signals. The main difference is due to the differences in the boundary conditions for the three parameters discussed above. Indeed, the normal current component vanishes at the ground surface because the atmosphere is insulating, surface temperature is usually constant and we have an open boundary condition for the CO₂ flux at the ground surface.

High concentration of CO₂ demonstrates the upflow of hydrothermal fluids. In contrast, the absence of anomalous CO₂ concentration in the ‘Small Fossa crater’ (Fig. 3), at only 50–150 m from the magmatic conduits, indicates that this sector is sealed from the underlying hydrothermal system. Precipitation/dissolution chemistry in the hydrothermal system could be responsible for the existence of compartments such as those demonstrated in the last decade in sedimentary basins (Ortoleva 1994) and at the Vulcano crater (Stix *et al.* 1993; Fischer *et al.* 1996; Chébli 1997). Fluid flow is possible only in areas where the existence of cracks, episodically reactivated, exist to serve as preferential pathways for the upflow of the hydrothermal fluids. These preferential pathways are located at the rims of the various craters in the Fossa area. A comparison of the different methods indicates that CO₂ represents the most sensitive method for identifying the escape of hydrothermal fluids. Indeed, CO₂ anomalies related to the Pizzo crater and the Sciara del Fuoco sector collapse have no self-potential and temperature counterparts (Fig. 4).

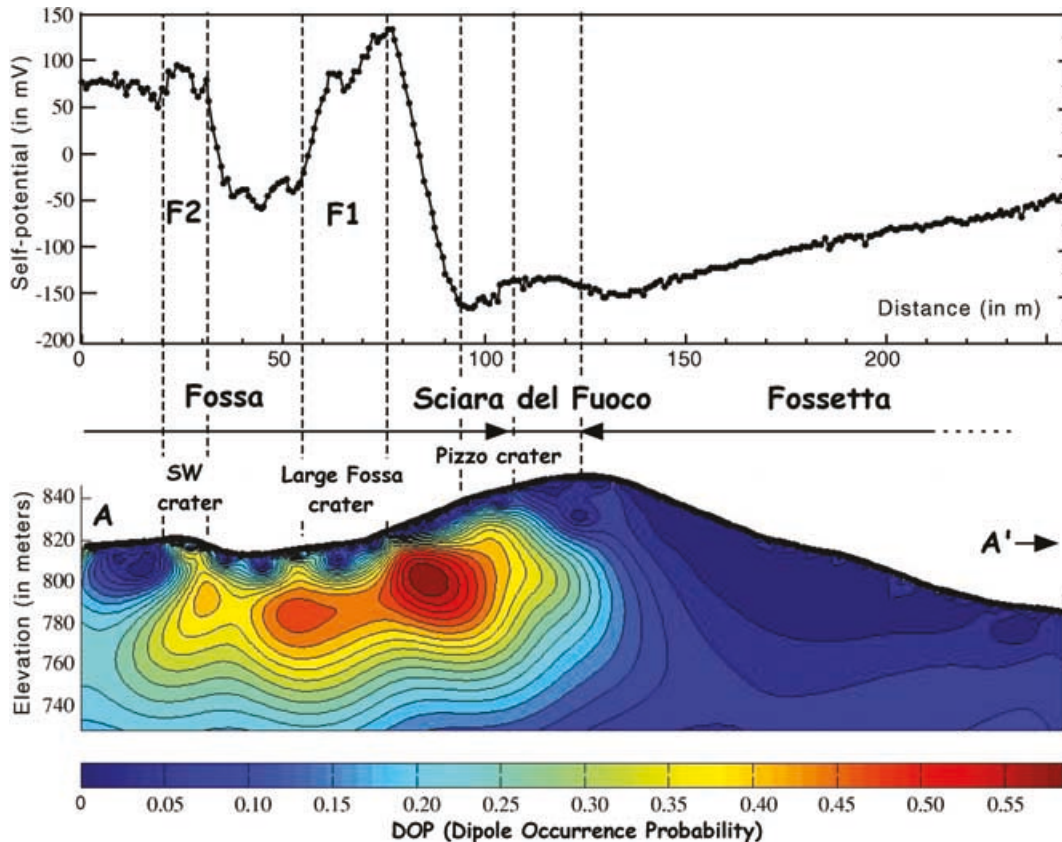


Figure 11. The dipole occurrence probability (DOP) tomography of the self-potential sources along the AA' profile.

5 RELATION WITH PAROXYSMAL ACTIVITY

5.1 Threats of phreato-magmatic eruptions

As mentioned above, geophysical and geochemical data demonstrate the presence of a perched aquifer located inside the Small Fossa crater. This perched aquifer collects (1) the water from the drainage network extending from the thermal anomalies (and their associated uprise of hydrothermal fluids) to the Small Fossa crater, Fig. 3), and (2) the meteoric water (the rains do not generate any surface flows at Stromboli as the water penetrates the permeable ground quickly). This existence of this perched aquifer, located only ~ 100 m away from the active magmatic conduits, could have strong consequences for the occurrence of mild explosive activity in the case of magma–water interaction. Drastic morphological changes of the volcano in the past were associated with paroxysmal eruptions with a phreato-magmatic origin (e.g. Rittmann 1931). The same type of phenomenon could again threaten the island. So far, the various studies performed at Stromboli using different kinds of methods (seismic, acoustic, infrasonic, thermal monitoring, video monitoring and tilt measurements) have not allowed the observation of clear precursors of the strong eruptions (see Ripepe *et al.* 1996, 2001; Bertagnini *et al.* 1999; Ripepe & Gordeev 1999). Another candidate still to explore is the possibility of occurrence of electrical signals of an electrokinetic nature as precursors of the volcanic paroxysms now discussed.

5.2 Possible electrokinetic precursors of paroxysmal activity?

This question is related to the electrical behaviour of a water-saturated porous body under increase of the confining stress up to cracking. This problem has been investigated recently in the laboratory by Clint (1999) and Yoshida (2001). Clint (1999) showed that in water-saturated basaltic rocks, pre-seismic and co-seismic electrical signals exist when the stress is increased to the fracture limit of the sample (Fig. 12). The signals occurred during microcracking and shear fracturing with the growth of new dilatant cracks. Clint (1999) identified the electrokinetic effect as the major contributor to these signals, with the piezo-electric effect providing only a negligible contribution. The experiments performed by Clint (1999) showed that a low permeability basalt behaves, in a first stage of deformation, as a closed system in response to stress increase. This generates localized source current densities of an electrokinetic nature. When the permeability increases through the development of a network of connected cracks, the electrical potential is noticed to increase as fluid pathways become more and more interconnected. Clint (1999) observed that electrical signals were higher for drained than for undrained conditions.

These findings could be applied to the forecasting of the volcanic activity if phreato-magmatic effects are the origin of the major or paroxysmal eruptions at Stromboli volcano. A 2 MPa fluid pressure change is responsible for a source voltage difference of $\delta C \delta p = 200$ mV using $\delta C = 100 \text{ mV MPa}^{-1}$, which corresponds to a relative change of the electrokinetic coupling coefficient associated with cracking. If the process is relatively shallow, say < 250 m, which is also the depth of the magmatic chamber from seismic investigations (La Rocca *et al.* 2003), it would generate electrical potential changes that are perfectly detectable at the ground surface using a dedicated monitoring network.

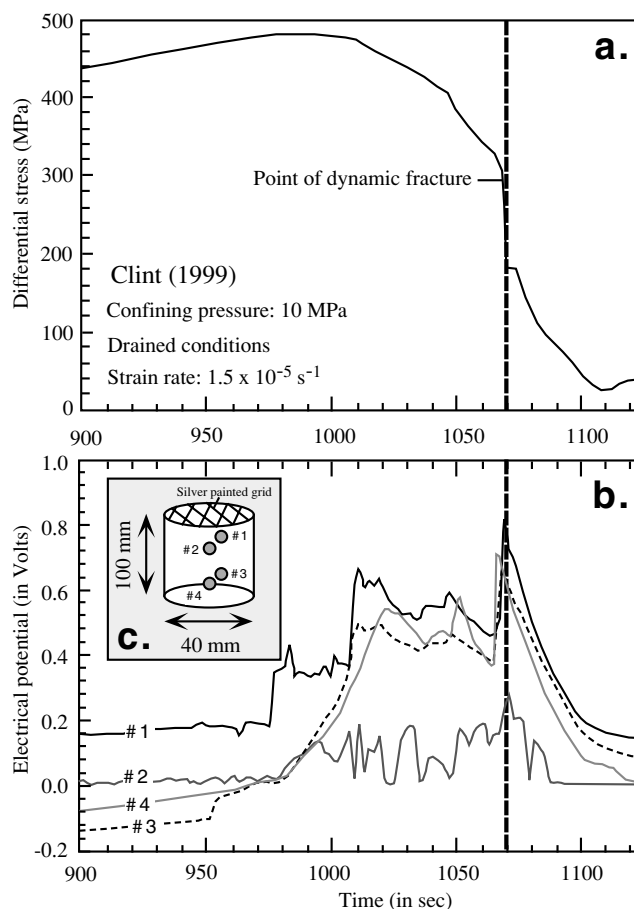


Figure 12. Electrical potential differences during strain softening and fracture for thermally cracked basalt (modified from Clint 1999, with permission). Note the electrical potential variations recorded during the phase of crack growth and linkage prior to the ultimate fracturation of the sample. These results indicate that electrical field disturbances are expected before a phreato-magmatic eruption. These disturbances can be recorded with a set of SP stations and inverted to recover the location of the source distribution of the dipolar moment.

These signals also have to be distinguished from the localized high-frequency self-potential variations recorded on Stromboli and in the laboratory by Büttner *et al.* (2000). Büttner *et al.* (2000) analysed highly transient electrical potential signals at approximately 100–200 m away from Stromboli active craters (several hundreds of ms and a few tens of mV in magnitude) and resulting from thermohydrodynamic fragmentation of the magma. The signals we are looking for would have a smaller frequency and should be observable far away from the magmatic conduits.

An obvious source of noise corresponds to the infiltration of water associated with raining. Such a signal can be identified with the meteorological stations available at the top of Stromboli. As discussed in Section 2, atmospheric electrical field variations could also have an influence especially during magnetic storms when electrical signals can be clearly dominated by magneto-telluric induction phenomena (e.g. Perrier & Morat 2000; Trique *et al.* 2002). Trique *et al.* (2002) reported variations in the range $1-10^3 \mu\text{V m}^{-1}$ and controlled by the shallow electrical resistivity distribution. The main structural contact between the hydrothermal system and the surrounding rocks observed here would channel the electrotelluric currents due to strong (two orders of magnitude) electrical resistivity contrasts. To remove this kind of temporal variation, electrical

measurements need to be combined with magnetic measurements. Corrections can be accomplished, for example, by filtering the self-potential measurements with specific filters based on the magnetic variations recorded with a magnetometer and a reference station for the self-potential survey. A complete set of magnetotelluric stations would be necessary so that electric and magnetic variations and their dependence on volcanic activity could be observed. Changes in the conductivity structure of the subsurface could be investigated as well as those associated with cracking and flow of hot hydrothermal fluids inside the hydrothermal plumbing system of the volcano.

The knowledge of the geometry of the hydrothermal plumbing system is also fundamental to install such a monitoring network. Indeed, the electrical response to ground water flow will be more contrasted if the two electrodes forming a measurement dipole are located above areas with very different hydraulic connectivity. The installation of a monitoring network spreading over a permeability barrier appears as an opportunity to study any variation of the hydraulic flux related to thermohydro-mechanical disturbances. Other dipoles need to be installed outside the hydrothermal outflow areas with a distribution that would allow inversion of the self-potential data in terms of source location (such as in seismology). For this purpose the type of algorithm described in the Appendix would be more useful than in the purpose of analysing the static self-potential profile due to the discreteness of the source distribution in the former case. This will form the basis for future monitoring operations at Stromboli volcano.

6 CONCLUDING STATEMENTS

The extensive study described in this work complements previous works by Finizola *et al.* (2003) in describing the pattern of ground water flow in the Fossa area of Stromboli volcano. Pertinent information is gained from electrical resistivity tomographies concerning the preferential fluid flow pathways in the plumbing system and the existence of domains sealed by low-permeability formations. The existence of a shallow unconfined aquifer at ~20 m below the topographic low of the Small Fossa crater is suggested by various measurements. The existence of this aquifer, located in the vicinity of the active vents, represents a major threat that could explain the occurrence of major or paroxysmal events at Stromboli. The next step concerns the installation of a monitoring network in the Fossa area including electrical dipoles and temperature probes with automatic measurements systems (data loggers). This network will be used to detect possible electrical precursors of the major or paroxysmal eruptions. In addition, 3-D electrical resistivity tomography is required to a depth of ~250 m to image the magmatic body, the hydrothermal plumbing system and the extent of the perched aquifer located in the Small Fossa crater.

ACKNOWLEDGMENTS

We are grateful to Nicolas Fournier and Andy Harris for their help during the 2002 May international research effort on Stromboli volcano. We thank the Ministère de l'Éducation Nationale de la Recherche (MENRT) in France (ACI Jeune to A. Revil and ACI 'Eau et Environnement' to A. Revil and D. Gibert) and the French National Research Council (CNRS). B. Dupré, M. Cara, J.F. Lénat, P. Choukroune and B. Hamelin are thanked for their support. We thank Ole Hanekop and Karsten Bahr for their constructive comments.

REFERENCES

Aubert, M. & Atangana, Y., 1996. Self-potential method in hydrogeological exploration of volcanic areas, *Ground Water*, **34**, 1010–1016.

- Aubert, M. & Baubron, J.C., 1988. Identification of a hidden thermal fissure in a volcanic terrain using a combination of hydrothermal convection indicators and soil-atmosphere analysis, *J. Volc. Geotherm. Res.*, **35**, 217–225.
- Aubert, M. & Dupuy, J.C., 2000. Geophysics and hydrogeology in volcanoclastic rocks, in *Volcanoclastic Rocks, from Magma to Sediments*, Vol. 13, pp. 253–266, eds Gordon and Breach, New York.
- Aubert, M., Antraygues, P. & Soler, E., 1993. Interprétation des mesures de polarisation spontanée (PS) en hydrogéologie des terrains volcaniques. Hypothèses sur l'existence d'écoulements préférentiels sur le flanc Sud du Piton de la Fournaise (Ile de la Réunion), *Bull. Soc. Géol. France*, **164**, 17–25.
- Ballestracci, R., 1982. Self-potential survey near the craters of Stromboli volcano (Italy). Inference for internal structure and eruption mechanism, *Bull. Volcanol.*, **45**, 349–365.
- Barberi, F., Rosi, M. & Sodi, A., 1993. Volcanic hazard assessment at Stromboli based on review of historical data, *Acta Vulcanol.*, **3**, 173–187.
- Barberi, F., Carapezza, M.L., Alean, J. & Carniel, R., 2001. Major explosion at Stromboli kills a tourist on 20 October 2001, *Bull. Glob. Volc. Net.*, **26**, 2–3.
- Bernabé, Y., 1998. Streaming potential in heterogeneous networks, *J. geophys. Res.*, **103**, 20 827–20 841.
- Bertagnini, A., Coltelli, M., Landi, P., Pompilio, M. & M. Rosi, 1999. Violent explosions yield new insights into dynamics of Stromboli volcano, *EOS, Trans. Am. geophys. Un.*, **80**, 633–636.
- Boubekraoui, S., Courteaud, M., Aubert, M., Albouy, Y. & Coudray, J., 1998. New insights into the hydrogeology of a basaltic shield volcano, from SP and electromagnetic data, The case history of the Piton de la Fournaise, Indian Ocean, *J. appl. Geophys.*, **40**, 165–177.
- Büttner, R., Zimanowski, B. & Röder H., 2000. Short-time electrical effects during volcanic eruption: experiments and field measurements, *J. geophys. Res.*, **105**, 2819–2827.
- Chébli, Y., 1997. Tomographie thermique et géoélectrique du cratère du Vulcano, *Mémoire de D.E.A. Processus Magmatiques et Métamorphiques—Volcanologie*, p. 60, Université Blaise Pascal, Clermont-Ferrand II.
- Clint, O.C., 1999. Electrical potential changes and acoustic emissions generated by fracture and fluid flow during experimental triaxial rock deformation, PhD thesis, p. 236, University College London.
- Di Maio, R. & Patella, D., 1994. Self-potential anomaly generation in volcanic areas. The Mount Etna case history, *Acta Vulcanologica*, **4**, 119–124.
- Di Maio, R., Di Sevo, V., Giammetti, S., Patella, D., Piscitelli, S. & Silenziario, C., 1996. Self-potential anomalies in some Italian volcanic areas, *Ann. Geofis.*, **39**, 179–188.
- Finizola, A., Sortino, S., Lénat, J.-F. & Valenza, M., 2002. Fluid circulation at Stromboli volcano (Aeolian Islands, Italy) from self-potential and CO₂ surveys, *J. Volc. Geotherm. Res.*, **116**, 1–18.
- Finizola, A., Sortino, S., Lénat, J.-F., Aubert, M., Ripepe, M. & Valenza, M., 2003. The summit hydrothermal system of Stromboli. New insights from self-potential, temperature, CO₂ and fumarolic fluid measurements. Structural and monitoring implications, *Bull. Volcanol.*, **65**, 486–504, doi:10.1007/s00445-003-0276-z.
- Fischer, T.P., Arehart, G.B., Sturchio, N.C. & Williams, S.N., 1996. The relationship between fumarole gas composition and eruptive activity at Galeras Colcano, Columbia, *Geology*, **24**, 531–534.
- Fournier, C., 1989. Spontaneous potentials and resistivity surveys applied to hydrogeology in a volcanic area: case history of the Chaîne des Puys, *Geophys. Prospect.*, **37**, 647–668.
- Gibert, D. & Pessel, M., 2001. Identification of sources of potential fields with the continuous wavelet transform: application to self-potential profiles, *Geophys. Res. Lett.*, **28**, 1863–1866.
- Jackson, D.B. & Kauahikaua, J., 1987. Regional self-potential anomalies at Kilauea volcano, 'Volcanism in Hawaii' chapter 40 USGS Professional paper **1350**, 947–959.
- Jaupart, C. & Vergnolle, S., 1988. Laboratory models of Hawaiian and Strombolian eruptions, *Nature*, **331**, 58–60.

- Jaupart, C. & Vergnolle, S., 1990. The generation and collapse of a foam layer at the roof of a basaltic magma chamber, *J. Fluid Mech.*, **203**, 347–380.
- Johnston, M.J.S., Byerlee, J.D. & Lockner, D., 2001. Rapid fluid disruption: a source for self-potential anomalies on volcanoes, *J. geophys. Res.*, **106**, 4327–4335.
- Jouniaux, L., Bernard, M.-L., Zamora, M. & Pozzi, J.-P., 2000. Streaming potential in volcanic rocks from Mount Pelée, *J. geophys. Res.*, **105**, 8391–8401.
- La Rocca, M., Saccorotti, G., Del Pezzo E. & Ibanez, J., 2003. Probabilistic source location of explosion quakes at Stromboli volcano estimated with multiple array data, *J. Volcanol. Geotherm. Res.*, **131**, 123–142.
- Lewicki, J.L., Connor, C., St-Amand, K., Stix, J. & Spinner, W., 2003. Self-potential, soil CO₂ flux, and temperature on Masaya volcano, Nicaragua, *Geophys. Res. Lett.*, **30**, 1817, doi:10.1029/2003GL017731.
- Llera, F.J., Sato, M., Nakatsuka, K. & Yokoyama, H., 1990. Temperature dependence of the electrical resistivity of water-saturated rocks, *Geophysics*, **55**, 576–585.
- Loke, M.H. & Barker, R.D., 1996. Rapid least-squares inversion of apparent resistivity pseudosections by a quasi-Newton method, *Geophys. Prospect.*, **44**, 131–152.
- Métrich, N., Bertagnini, A., Landi, P. & Rosi, M., 2001. Crystallisation driven by decompression and water loss at Stromboli volcano (Aeolian Island), *J. Petrol.*, **42**, 1471–1490.
- Ortoleva, P.J., 1994. *Basin Compartments and Seals*, AAPG Memoir 61, Tulsa, 3–26, p. 477.
- Patella, D., 1997. Self-potential global tomography including topographic effects, *Geophys. Prospect.*, **45**, 843–863.
- Perrier, F. & Morat, P., 2000. Characterization of electrical daily variations induced by capillary flow in the non-saturated zone, *Pure appl. Geophys.*, **157**, 785–810.
- Poldini, E., 1938. Geophysical exploration by spontaneous polarisation methods, *Mining Mag.*, London, **59**, 278–282, 347–352.
- Revil, A., 2002a. Comment on ‘Rapid fluid disruption: a source for self-potential anomalies’ by Johnston, M.J.S., *et al.*, *J. geophys. Res.*, **107**, doi:10.1029/2001JB000788.
- Revil, A., 2002b. The hydroelectric problem of porous rocks: thermodynamic approach and introduction of a percolation threshold, *Geophys. J. Int.*, **151**, 944–949.
- Revil, A., Naudet, V., Nouzaret, J. & Pessel, M., 2003a. Principles of electrography applied to self-potential electrokinetic sources and hydrogeological applications, *Water Resources Res.*, **39**, doi:10.1029/2001WR000916.
- Revil, A., Saracco, G. & Labazuy, P., 2003b. The volcano-electric effect, *J. geophys. Res.*, **108**, doi:10.1029/2002JB001835.
- Ripepe, M. & Gordeev, E., 1999. Gas bubble dynamics model for shallow volcanic tremor at Stromboli, *J. geophys. Res.*, **104**, 10 639–10 654.
- Ripepe, M., Poggi, P., Braun T. & Gordeev, E., 1996. Infrasonic waves and volcanic tremor at Stromboli, *Geophys. Res. Lett.*, **23**, 181–184.
- Ripepe, M., Ciliberto, S. & Schiava, M.D., 2001. Time constraints for modeling source dynamics of volcanic explosions at Stromboli, *J. geophys. Res.*, **106**, 8713–8727.
- Rittmann, A., 1931. Der Ausbruch des Stromboli am 11 September 1930, *Zeits. Vulkanol.*, **14**, 47–77.
- Trique, M., Richon, P., Perrier, F., Avouac, J.P. & Sabroux, J.C., 1999. Radon emanation and electric potential variations associated with transient deformation near reservoir lakes, *Nature*, **399**, 137–141.
- Trique, M., Perrier, F., Froidefond, T., Avouac, J.P. & Hautot, S., 2002. Fluid flow near reservoir lakes inferred from the spatial and temporal analysis of the electric potential, *J. geophys. Res.*, **107**, 10.1029/2001JB000482.
- Yoshida, S., 2001. Convection current generated prior to rupture in saturated rocks, *J. geophys. Res.*, **106**, 2103–2120.
- Zlotnicki, J. & Le Mouél, J.L., 1988. Volcanomagnetic effects observed on Piton de la Fournaise Volcano (Réunion Island): 1985–1987, *J. geophys. Res.*, **93**, 9157–9171.
- Zohdy, A.A., Anderson, L.A. & Muffler, L.J.P., 1973. Resistivity, self-potential, and induced-polarisation surveys of a vapor-dominated geothermal system, *Geophysics*, **38**, 1130–1144.

APPENDIX

Here we propose a dipolar tomography to identify the depth location of the self-potential sources. This tomographic approach is the natural extension of the monopole tomography approach of Patella (1997) (see also Gibert & Pessel 2001). The electrical potential φ (in V) at the observation station P is represented as a sum of Q electrostatic dipoles in a homogeneous rock volume:

$$\varphi_q(P) = \sum_{q=1}^Q \frac{p_q}{4\pi\epsilon r_q^2} [\cos(\theta_q + \psi_q)], \quad (\text{A1})$$

$$\varphi_q(P) = \sum_{q=1}^Q \frac{p_q}{4\pi\epsilon r_q^2} [\cos\theta_q \cos\psi_q - \sin\theta_q \sin\psi_q], \quad (\text{A2})$$

where p_q is the dipole moment of source q (in C m), ψ_q and θ_q are two angles characterizing the direction of this dipolar source with the vertical axis and the direction of the vector S_qP with the vertical axis (Fig. 10), ϵ is the dielectric constant of the medium (in F m⁻¹) and r_q is the distance (in m) between the dipole q and the observation point $P[x, z(x)]$, $z(x)$ represents the topography of the ground surface, and (x_q, z_q) are the coordinates of the q th source. The self-potential measured along the local curvilinear coordinate u at point P located at the ground surface (outside the source volume containing the primary sources) can be written as the sum of Q discrete electrical dipoles located in depth. This yields

$$\varphi(P) = - \sum_{q=1}^Q \frac{\Gamma_{q,1}(x - x_q) + \Gamma_{q,2}[z(x) - z_q]}{\{(x - x_q)^2 + [z(x) - z_q]^2\}^{3/2}}, \quad (\text{A3})$$

$$\Gamma_{q,1} \equiv \frac{p_q \sin\psi_q}{4\pi\epsilon}, \quad (\text{A4})$$

$$\Gamma_{q,2} \equiv \frac{p_q \cos\psi_q}{4\pi\epsilon}, \quad (\text{A5})$$

where $\Gamma_{q,1}$ and $\Gamma_{q,2}$ (in V m²) are the intensities of the horizontal and vertical components of the q th source dipole, respectively ($\Gamma_{q,1} = 0$ for a vertical dipole, $\psi_q = 0, \pi$, whereas $\Gamma_{q,2} = 0$ for a horizontal dipole, $\psi_q = \pi/2, -\pi/2$). The electrical field at point P along the profile is given by

$$E_u(P) \equiv - \frac{\partial\varphi(P)}{\partial u} = - \left(\frac{\partial\varphi}{\partial x} + \frac{\partial\varphi}{\partial z} \frac{dz}{dx} \right) \frac{dx}{du}, \quad (\text{A6})$$

$$E_u(P) = \sum_{q=1}^Q (\Gamma_{q,1} \mathfrak{S}_{u,1} + \Gamma_{q,2} \mathfrak{S}_{u,2}), \quad (\text{A7})$$

where u is the curvilinear coordinate of point P along the self-potential profile describing the ground surface, dz/dx is the slope effect of the curvilinear elevation profile describing the ground surface. The two scanning functions $\mathfrak{S}_{u,k}$, $k \in \{1, 2\}$, are:

$$\begin{aligned} \mathfrak{S}_{u,1}(x - x_q, z(x) - z_q) &= \frac{[-2(x - x_q)^2 + (z - z_q)^2 - 3(dz/dx)(x - x_q)(z - z_q)]}{[(x - x_q)^2 + (z - z_q)^2]^{5/2}} \left(\frac{dx}{du} \right), \end{aligned} \quad (\text{A8})$$

$$\begin{aligned} \mathfrak{S}_{u,2}(x - x_q, z(x) - z_q) &= \frac{\{-3(x - x_q)(z - z_q) + (dz/dx)[-2(z - z_q)^2 + (x - x_q)^2]\}}{[(x - x_q)^2 + (z - z_q)^2]^{5/2}} \\ &\times \left(\frac{dx}{du} \right). \end{aligned} \quad (\text{A9})$$

For a flat ground surface, the scanning functions are directly obtained by taking $dx/du = 1$ and $dz/dx = 0$ in eqs (13) and (14). The 2-D tomography is based on a cross-correlation algorithm between the theoretical scanning functions $\mathfrak{S}_{u,k}$, $k \in \{1, 2\}$ and the electrical self-potential field E_u recorded at the ground surface in order to determine the most probable distribution of discrete dipoles at depth responsible for the self-potential anomaly observed at the ground surface. A horizontal dipole occurrence probability (HDOP-) η_1 and a vertical dipole occurrence probability (VDOP-) η_2 are determined for such a purpose,

$$\eta_k(x_q, z_q) = C_k \int_{-\infty}^{+\infty} E_u[x, z(x)] \mathfrak{S}_{u,k}[x - x_q, z(x) - z_q] dx, \quad (\text{A10})$$

$$C_k \equiv \left\{ \int_{-\infty}^{+\infty} E_u^2[x, z(x)] dx \int_{-\infty}^{+\infty} \mathfrak{S}_{u,k}^2[x - x_q, z(x) - z_q] dx \right\}^{-1/2}, \quad (\text{A11})$$

where $k \in \{1, 2\}$, C_1 and C_2 are normalization factors, which include a normalization by the total power of the electrical field recorded at the ground surface. The integrals in eqs (15) and (16) can be numerically evaluated since they are only related to the electrical field at the ground surface, which can be computed directly from the self-potential profile, and the scanning functions given by eqs (13) and (14). We have $-1 \leq \eta_1(x_q, z_q) \leq 1$ and $-1 \leq \eta_2(x_q, z_q) \leq 1$ and as $\text{sign}[\eta_1(x_q, z_q)] = \text{sign}(\Gamma_{q,1})$, the case $\eta_1 > 0$ corresponds to a dipole contribution oriented in the right-hand side ($\psi_q \in [0, \pi]$) according to the convention taken in Fig. 10, $\eta_1 < 0$ corresponds to a dipole contribution oriented in the left-hand side ($\psi_q \in [-\pi, 0]$). The case $\eta_2 > 0$ corresponds to a dipole contribution oriented upward ($\psi_q \in [-\pi/2, \pi/2]$) and $\eta_2 < 0$ corresponds to a dipole contribution oriented downward ($\psi_q > \pi/2$ or $\psi_q < -\pi/2$). In addition, a dipole occurrence probability (DOP) function and a phase angle are defined by

$$\eta(x_q, z_q) = \sqrt{\eta_1^2(x_q, z_q) + \eta_2^2(x_q, z_q)}, \quad (\text{A12})$$

$$\theta(x_q, z_q) = \arctan[\eta_2(x_q, z_q)/\eta_1(x_q, z_q)], \quad (\text{A13})$$

respectively, with the property $0 \leq \eta(x_q, z_q) \leq 1$. The DOP function represents the probability of finding in a point (x_q, z_q) of the subspace Ω a dipole responsible for the self-potential anomaly observed at the ground surface. The subsurface is divided into elements. The HDOP, VDOP and DOP functions attached to each element are determined from the self-potential data recorded at the ground surface and the equations provided above. Then these values are contoured to provide a tomographic image of the probable location of the dipole occurrence in the subsurface. The dipole occurrence probability $\eta(x_q, z_q)$ provides a tool for source recognition associated with a discrete dipolar polarization at depth. However, such a tomographic approach should be used with great care as for example it is not suitable for extended source distributions due to the aliasing of the self-potential data recorded at the ground surface.

We now investigate the electrical response of ground water flow in a confined aquifer. The electrical potential at the observation station P located at the ground surface is (Revil *et al.* 2003b)

$$\varphi(P) = \frac{1}{2\pi} \int_{\Omega} \left(\frac{C\eta_f}{\rho_f k} \right) \frac{\nabla \cdot (\rho_f \mathbf{u})}{r} dV, \quad (\text{A14})$$

where r represents the distance between the observation point P and the infinitesimal volume element dV of the conductive medium surrounding the integration source point M . We consider a confined and homogeneous aquifer in which steady state ground water flow takes place. For steady-state flow, the flow pattern is characterized by $\nabla \cdot (\rho_f \mathbf{u}) = \rho_f \underline{Q}$, where \underline{Q} (in s) represents the source of water per unit volume and per unit time generated inside the control volume. For a confined aquifer under steady-state conditions, $\underline{Q}(\mathbf{r}) = 0$ except at the inflow and outflow areas of the confined aquifer. So free convection in a confined homogeneous aquifer does not provide any electrical field source for an observation point located at the ground surface except in the inflow and outflow areas.